Multi-mirror adaptive optics for control of thermally induced aberrations in extreme ultraviolet lithography

Habets, Michel; Scholten, Joni; Weiland, Siep; Coene, Wim

DOI
10.1117/12.2219168

Publication date
2016

Document Version
Final published version

Published in
Extreme Ultraviolet (EUV) Lithography VII

Multi-Mirror Adaptive Optics for Control of Thermally Induced Aberrations in Extreme Ultraviolet Lithography

Michel Habets[a], Joni Scholten[a], Siep Weiland[a], and Wim Coene[b]

[a]Department of Electrical Engineering, Eindhoven University of Technology, P.O. Box 513, 5600 MB Eindhoven, The Netherlands
[b]Department of Imaging Science and Technology, Faculty of Applied Sciences, Delft University of Technology, P. O. Box 5046, 2600 GA Delft, The Netherlands

ABSTRACT

The imaging quality of the projection optics of an extreme ultraviolet lithography scanner degrades under the influence of thermally induced deformations of its mirrors. Wavefronts of different reticle points encounter different parts of the deformed mirrors, resulting in a field dependent wavefront error. This paper presents how ideas from multi-conjugate adaptive optics can be used to reduce these thermally induced aberrations. To this end a generic deformable mirror model is implemented. Linear actuator sensitivities are derived directly, based on nominal ray locations and directions, enabling fast prototyping. An integrated opto-thermo-mechanical mirror heating model is used to determine the evolution of thermally induced abberations over time. This transient simulation is used to analyze four different adaptive optics configurations and two different control algorithms. It is shown that by employing the multi-objective goal-attainment method, it is possible to improve the optical performance significantly when compared to minimizing the ℓ_2-norm of the total residual wavefront error vector.

Keywords: Thermally induced aberrations, Mirror heating, Aberration control, Adaptive optics, Deformable mirrors, EUV Lithography

1. INTRODUCTION

Extreme ultraviolet lithography (EUVL) is widely considered to be the prime technology that will continue cost-effective shrinking of semiconductor feature sizes in the near future.[1,2] Since EUV light is strongly absorbed by most materials, EUVL operates in vacuum and uses reflective instead of refractive optics. In this paper we consider a so-called projection optics box (POB) that transmits the light from the reticle to the wafer via six multilayer coated mirrors. These mirrors absorb roughly 35 % of the incoming light, which causes them to heat up. The use of off-axis illumination causes localized heating at small regions near the edge of the pupil, resulting in undesired deformations of the mirrors. In turn, these deformations lead to thermally induced aberrations known as mirror heating.

In the coming years, it is possible to mitigate mirror heating by means of rigid body adjustments of mirrors and stages. However, with an increase of source power and increased use of extreme off-axis illumination, mirror heating might be an issue that requires additional measures. Several papers and theses have addressed this topic by applying adaptive optics (AO) to counteract the thermally induced aberrations in EUVL machines.[3,4] Traditionally, the focus has always been on classical AO,[5] where a single deformable mirror (DM) is placed at the position of the aperture stop. This compensation is only efficient for a limited part of the field, because the thermally induced aberrations are field dependent. This dependency originates from the fact that different field points encounter different parts of the deformed mirrors when traveling through the POB.

In order to address the limited field correctability of classical AO, we investigate the possibility of controlling the thermally induced aberrations by means of multiple deformable mirrors, referred to as multi-mirror adaptive optics (MMAO). This approach is similar to multi-conjugate adaptive optics (MCAO), which is often used in

Further author information: (Send correspondence to Michel Habets)
Michel Habets: E-mail: m.b.i.habets@tue.nl, Telephone: +31 40 247 3142

Extreme Ultraviolet (EUV) Lithography VII, edited by Eric M. Panning, Kenneth A. Goldberg. Proc. of SPIE Vol. 9776, 97762D · © 2016 SPIE · CCC code: 0277-786X/16/$18 · doi: 10.1117/12.2219168

astronomical telescopes.[5,6] The assumption that additional deformable mirror surfaces improve the performance is supported by literature on MCAO.[7]

The aim of this study is twofold. First, we evaluate different MMAO configurations by means of a simulation model of a patented POB design.[8] Although this design is not used in current production machines, it does provide a realistic simulation model. Second, we aim to provide a control algorithm for MMAO. In addition to minimizing the residual phase variance, we use a multi-objective optimization strategy that is capable of directly taking design specific imaging criteria into account.

To reach these aims we implemented a generic deformable mirror model, that enables fast prototyping. To investigate the effect of the deformable mirror on the wavefront, we used a linearized model. This model describes a direct relation between the deformed mirror surface on the one hand and the resulting wavefront error on the other hand. A previously developed[9] integrated opto-thermo-mechanical mirror heating model was used to determine the evolution of the thermally induced deformation over time. Based on wavefront error (WFE) measurements a controller action is derived at each measurement instant. To quantify the performance of the controlled POB, each measured WFE is assessed based on three properties: RMS WFE and local centroid distortion in x and y coordinates.

The remainder of this paper is organized as follows: Section II provides an overview of the modeling framework and details on the simulated use case. Next, section III introduces the deformable mirror model and Section IV describes the construction of the influence functions. Section V explains the various optimization procedures explored. Simulation results are given in section VI. Finally, Section VII provides the conclusions.

2. MODELING FRAMEWORK AND USE CASE SPECIFICATION

In this chapter we provide details on our modeling framework and the use case that is used throughout this paper. The integrated opto-thermo-mechanical mirror heating model has been used in our previous study.[9] For completeness, we repeat the basic modeling assumptions in Section 2.1 and Section 2.2.

2.1 Projection optics for EUVL

The results presented in this paper are obtained from software simulations on an EUVL POB design from patent literature.[8] This system, for which NA = 0.25, consists of 6 mirrors and operates at a wavelength $\lambda = 13.5$ nm. A schematic of the optical system is depicted in Figure 1. Although this design differs from that in current production machines, it is sufficiently representative for the purpose of this study. The ring field has a radius of 30 [mm], a width of 2 [mm] and chord of 26 [mm] at the wafer plane, as shown in Figure 1. The aperture stop (AS) is located at mirror M2. All optical elements, from reticle to wafer have six rigid body degrees of freedom, except M5 and those mirrors that are implemented as a DM. From now on, we will call translations and tilts of the mirrors and stages: rigid body adjustments (RBA). Translations are in the direction of the global x, y, and z-axis. Rotations are around axes that are parallel to the global coordinate axis and originate at the mirror's center of clear aperture. The center of the clear aperture is defined as the point of intersection of the mirror surface with the chief ray from the central point of the ring field.

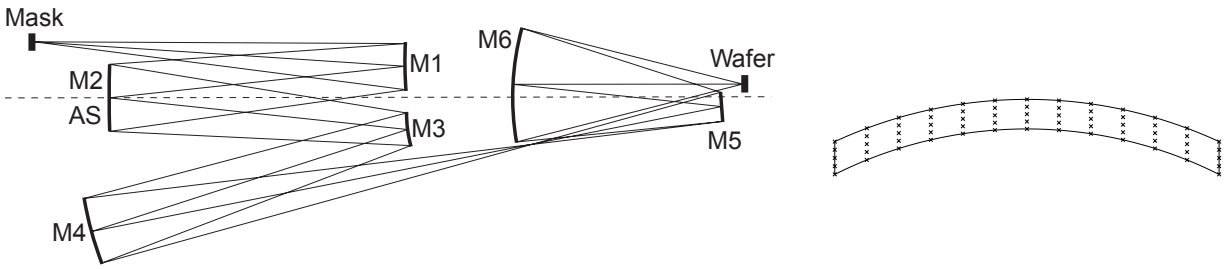

Figure 1: 2D schematic layout of six mirror projection optics and its ring field with 5×13 field points.

2.2 Integrated opto-thermo-mechanical mirror heating model

Thermally induced aberration predictions are based on a fully coupled multiphysics model of the POB. The thermal and mechanical analysis of the POB is performed with the aid of Finite Element Analysis (FEA). In particular, we use the software packages COMSOL Multiphysics. The mirror geometries are constructed based on the optical design prescription of the POB.[8] The mirror's clear aperture areas are extruded to obtain 3D models of the mirrors. The mirror substrate material is Ultra Low Expansion (ULE) glass with a nonlinear coefficient of thermal expansion (CTE) of 1.5 [ppb/K^2]. The zero-crossing temperatures (ZCT) are optimized for correctability at steady state. The Mo/Si multilayer coating of the mirrors have a thickness of a few microns and has been ignored. The mechanical boundary conditions are chosen such that thermal loads cause no internal stresses.

The heat load on each mirror depends strongly on diffraction of the structures on the mask and the illumination settings. In our simulations we consider off-axis y-dipole illumination of a dense line pattern. Each mirror absorbs EUV light at clear aperture and radiates heat outwards on all other sides.

The mirror deformations are calculated in the FEA and then passed to in-house software to perform the optical analysis of the heated POB. The surface deformations are interpolated and added to the optical prescription of the cold POB. A grid of 32×32 rays is traced for each of the $5 \times 13 = 65$ object points within the ring field (Figure 1) to obtain the wavefront maps of the heated POB.

2.3 Use case specification

To test the methods described in this paper, a use case that simulates imaging a dense pattern of lines and spaces is used. Specific parameters for this use case are specified in table 1. In practice, bounds on key performance indicators (KPI) depend on the specific design of the IC that is being produced. The proposed method does allow the inclusion of design specific imaging criteria based on, for instance, specific Zernike modes. However, for this paper, the KPI are limited to RMS WFE and centroid distortion in both x and y. The goals used are summarized in table 2. The ultimate goal is to get the KPI for each of the 65 object points below these bounds.

Table 1: Parameters of the simulated use case

Parameter	Unit	Value
Power at intermediate focus	W	1000
Pupil fill ratio		0.2
Pitch at the wafer	nm	40
y-dipole inner radius σ_i		0.64
y-dipole outer radius σ_o		0.9
y-dipole opening angle θ_o	rad	$\frac{\pi}{2}$
WFE sensor sampling time	s	30
Number of WFE measurements Q		65
Number of rays within pupil M		797

Table 2: Goals for the KPI

KPI	Nominal peak	Goal
RMS WFE	0.410 nm	0.675 nm
Centroid distortion length in x	0.462 nm	1.35 nm
Centroid distortion length in y	0.998 nm	1.35 nm

3. DEFORMABLE MIRROR MODEL

Simulating the capabilities of an MMAO corrected POB requires a model for its actuators. For this paper, the DM is assumed to be a piezo actuated DM. Initially, the exact number of piezo actuators is unknown, but is estimated at several hundreds. Deriving for each actuator the mechanical influence function based on finite element analysis is time-consuming. A simplified model for the mechanical influence function of a DM pixel would be very convenient at this stage. For this purpose, [10, p.357-358] suggests using a 2D Gaussian influence function:

$$g(\mathbf{x}) = \exp\left(\left(\frac{2||\mathbf{x}-\mathbf{r}||_2}{\text{FWHM}}\right)^2 \ln\left(\frac{1}{2}\right)\right), \quad \mathbf{r},\mathbf{x} \in \mathbb{R}^2 \tag{1}$$

in which $\mathbf{r}$ denotes the center position of the actuator and FWHM stands for Full Width Half Maximum. To get insight in whether this shape is indeed representative for a piezo DM, a rudimentary analysis has been carried out on a simplified solid mechanics model of M2 in COMSOL. In this model, each piezo actuator is modeled as a spring and a force. The actuators are placed on a hexagonal grid. This results in a more uniform actuator spacing and resulted in a better fit with the analytic model described by (1), when compared to placing the actuators on a Cartesian grid. Figure 2a shows the resulting influence function for the center actuator of M2 as generated by the COMSOL model. Figure 2b shows a cross-section of Figure 2a and shows to what extent (1) is able to model the influence function. The part close to the actuator center fits well, but the tails show quite some offset. In the context of this paper however, the DM is not expected to produce a shape in which only one actuator is activated. Furthermore, by reproducing a realistic thermal deformation on the piezo actuator COMSOL model, and fitting the resulting surface onto the Gaussian actuator grid it is confirmed that the two models behave similar in that context. The relative RMS fit error lies in the order of 10^{-3} nm. Therefore, for this paper, the DM influence functions modeled by (1) are regarded accurate enough to test the performance of different MMAO configurations. The analytic model described by (1) is nonzero on its domain, which is $\mathbb{R}^2$, resulting in a dense influence matrix. By multiplying (1) with a window function, one can remove the insignificant entries and introduce sparsity in the actuator influence function matrix. To this end a broadened Hanning window is used [10, p.358]:

$$h(\mathbf{x}) = \begin{cases} 1 & \text{if } ||\mathbf{x}-\mathbf{r}||_2 \leq R \\ \frac{1}{2} + \frac{1}{2}\cos\left(\frac{2\pi||\mathbf{x}-\mathbf{r}||_2 - R}{S}\right) & \text{if } R \leq ||\mathbf{x}-\mathbf{r}||_2 \leq R+S \\ 0 & \text{otherwise} \end{cases} \tag{2}$$

This window is used with $R = \text{FWHM}$ and $S = \frac{1}{2}\text{FWHM}$. This means that the sinusoidal part of the window function starts when the Gaussian function is at 6.25% of its peak value.

4. THE INFLUENCE OF CORRECTIONS ON THE WAVEFRONT

Geometric ray tracing is mathematically relatively simple and, at the same time, captures several important optical characteristics reasonably well. However, using non-linear geometric ray tracing in the optimization algorithm itself would require many ray trace iterations, putting a burden on the simulation time. Therefore, a linearized model is used, which describes a direct relation between RBA and DM actuators on the one hand and WFE on the other. The main idea is to derive a sensitivity matrix $\mathbf{J}$, that describes for each actuator the influence it has on the WFE of each ray. For this paper, the WFE data is generated for Q object points from geometric ray trace data. Each object point $q \in \{1, \cdots, Q\}$ is defined by a unique coordinate pair $\mathbf{x}_o(q) \in \mathbb{R}^2$. For each of these points, M rays are traced. A ray is uniquely defined by the combination of object point coordinates $\mathbf{x}_o(q)$ and its pupil coordinates $\mathbf{x}_p(m) \in \mathbb{R}^2, m \in \{1, \cdots, M\}$. This procedure leads to a total of QM WFE pixels $w(\mathbf{x}_o(q), \mathbf{x}_p(m))$. For each object point its WFE pixels are stacked into a vector $\mathbf{w}_q$ and all these vectors are again combined into a vector $\mathbf{w}$

$$\mathbf{w}_q = \begin{bmatrix} w\left(\mathbf{x}_o(q), \mathbf{x}_p\left(1\right)\right) & \cdots & w\left(\mathbf{x}_o(q), \mathbf{x}_p\left(M\right)\right) \end{bmatrix}^T \in \mathbb{R}^M \tag{3}$$

$$\mathbf{w} = \begin{bmatrix} \mathbf{w}_1^T & \cdots & \mathbf{w}_Q^T \end{bmatrix}^T \in \mathbb{R}^{QM} \tag{4}$$

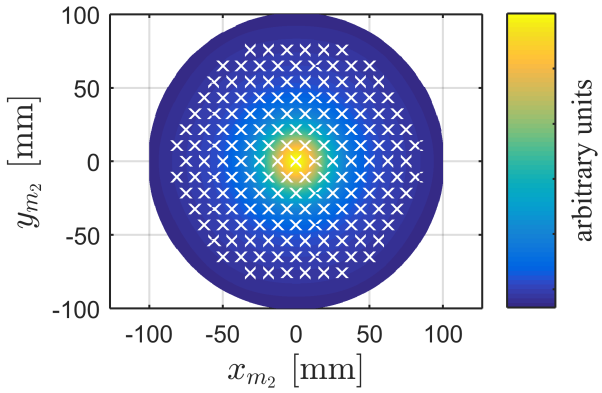

(a) Simulated influence function for the center actuator of M2 on a hexagonal grid with $\Delta_{act} = 11.8$ mm and a thickness of 28 mm. This result is obtained by runing a Solid Mechanics study in COMSOL. Crosses represent the actuator positions.

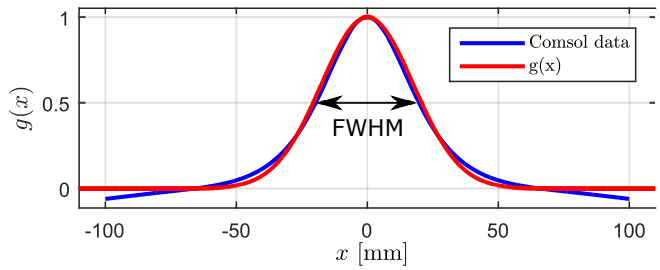

(b) Fit of a cross section of the influence function shown in fig. 2a with the Gaussian influence model. $\Delta_{act} = 11.8$ mm and a thickness of 28 mm. For these parameters, FWHM ≈ 40 mm.

Figure 2: Analysis of the Gaussian DM influence function model

The influence of the linear model, which from now on is called controller model, is described by the following equation

$$\tilde{\mathbf{w}} = \mathbf{J}\mathbf{c} \tag{5}$$

in which $\mathbf{c} = \begin{bmatrix} c_1 & \cdots & c_N \end{bmatrix}^T \in \mathbb{R}^N$ consists of all actuator commands (element translations, element tilts and DM pixel amplitudes) and $\tilde{\mathbf{w}}$ is the WFE correction, as calculated by the controller model. Furthermore, $\mathbf{J}$ is constructed as:[9–11]

$$\mathbf{J} = \begin{bmatrix} \frac{\partial \mathbf{w}}{\partial c_1} & \cdots & \frac{\partial \mathbf{w}}{\partial c_N} \end{bmatrix} \in \mathbb{R}^{QM \times N} \tag{6}$$

At each iteration the controller acts on the residual WFE:

$$\mathbf{w}_\epsilon = \mathbf{w} - \tilde{\mathbf{w}} \tag{7}$$

4.1 Influence functions for the Rigid Body Adjustments

The RBA sensitivities are calculated by analyzing geometric ray trace simulations for each actuator individually. For each of the $N_{rba} \leq N$ actuators, the optimal excitation value is determined by adjusting the actuator and analyzing the geometric ray trace data until the resulting RMS WFE is at a predefined value. Let the rth RBA actuator be denoted by the subscript n_r, where $n_r \in \{1, \cdots, N_{rba}\}$. Once the optimal value δ_{n_r} is determined, the rth RBA actuator is poked by $+\delta_{n_r}$ and then by $-\delta_{n_r}$. This results in two WFE vectors $\mathbf{w}_{+\delta_{n_r}}$ and $\mathbf{w}_{-\delta_{n_r}}$. These are then used in

$$\frac{\partial \mathbf{w}}{\partial c_{n_r}} \approx \mathbf{j}_{n_r} = \frac{\mathbf{w}_{+\delta_{n_r}} - \mathbf{w}_{-\delta_{n_r}}}{2\delta_{n_r}} \tag{8}$$

to calculate the sensitivity vector of the rth RBA actuator. The optimal value for δ_{n_r} is a trade-off between a small linearization interval and a high SNR in the derived actuator sensitivity.

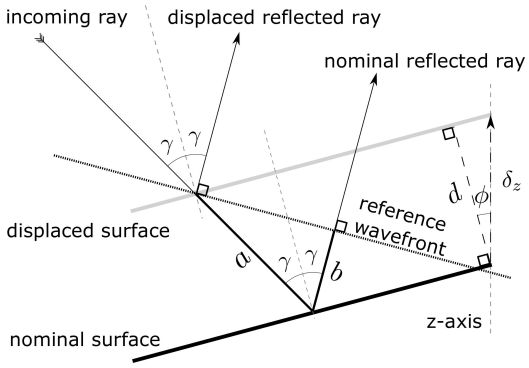

Figure 3: The effect of local surface tilt ϕ and angle of incidence γ on optical path length.

4.2 Influence functions for the Deformable Mirror pixels

Since several DM configurations have to be tested, deriving the influence function from simulation data for each DM actuator, as is done for the RBA actuators, will be time-consuming. Therefore, an analytic expression is favorable. In,[3] the influence of a local displacement along the z-direction on WFE is approximated by:

$$\tilde{w}_{dm}(\mathbf{x}_o, \mathbf{x}_p) = -2\delta_z \left(\mathbf{x}_{dm}(\mathbf{x}_o, \mathbf{x}_p)|_{\delta_z=0}\right) \tag{9}$$

Here $\delta_z(\mathbf{x}_{dm})$ is the local displacement of the reflecting surface along the z-axis. The z-component of the reflective surface normal points in the positive z-direction. Furthermore, $\mathbf{x}_{dm}(\mathbf{x}_o, \mathbf{x}_p)|_{\delta_z=0}$ represents the position at which the ray defined by the pair $(\mathbf{x}_o, \mathbf{x}_p)$ intersects with the reflecting surface under nominal conditions, so when $\delta_z = 0$.

More accurate modeling is possible, if one includes both the angle of incidence of a ray and the angle the local reflective surface normal makes with respect to the z-direction under nominal conditions.[12] To understand how both these angles act on the optical path length (OPL), one has to approach this problem from a wavefront perspective. Figure 3 shows a surface, before and after it is displaced along the z-axis over a distance δ_z. In both situations, the surface normal makes an angle ϕ with the z-axis. The incoming light ray hits both surfaces under an angle γ w.r.t. the surface normal. The difference in OPL is defined at the reference wavefront, which in this drawing is chosen at the point of intersection between the incoming ray and the displaced surface. By standard trigonometric formulas one can deduce that the change in OPL, which is the change in WFE, is given by

$$\tilde{w}_{dm} = -(a + b) = -2\cos(\phi)\cos(\gamma)\delta_z \tag{10}$$

Note that all variables depend on $\mathbf{x}_{dm}(\mathbf{x}_o, \mathbf{x}_p)|_{\delta_z=0}$ and in addition, γ also depends on the nominal incoming direction of a ray. These dependencies are omitted in (10) for readability.

5. CONTROL: OPTIMIZING THE PERFORMANCE OF THE THERMALLY DEFORMED PROJECTION OPTICS

Minimization of the Eucledian norm of the residual WFE $\mathbf{w}_\epsilon$ is used in most literature found on adaptive optics:[13, 14]

$$\mathbf{c}^* = \arg\min_{\mathbf{c}} ||\mathbf{w} - \mathbf{J}\mathbf{c}||_2 \tag{11}$$

where $\mathbf{c}^*$ defines the optimal control signal. Because in the context of this paper $QM > N$ a unique solution does not exist. In order to solve this ill-posed problem regularization techniques are frequently used. One way to avoid noise fitting and obey actuator constraints is Tikhonov regularization, which is often used in practice to improve the solution,[15] by adding a regularization matrix to 11 and solving

$$\mathbf{c}^* = \arg\min_{\mathbf{c}} ||\mathbf{w} - \mathbf{J}\mathbf{c}||_2 + ||\mathbf{\Gamma}\mathbf{c}||_2 \tag{12}$$

The most rudimentary implementation is to penalize large actuator values by setting $\Gamma = \alpha I \in \mathbb{R}^{N\times N}$. Another option is to penalize local derivatives of DM actuators, which is also called smoothing regularization [15, p.307]. This could be relevant, since a smooth surface is a useful property of a DM generated surface.

However, for this paper, the optimization is done by either formulating the problem as a constraint quadratic program (QP) for single objective-optimization, or by using the goal attainment (GA) method[16] for multi-objective optimization. Both problems are solved iteratively, using routines that contain stopping criteria. When the stopping criteria are tuned properly the need for regularization is reduced.

5.1 Single-objective optimization: Quadratic Programming

When (12) is solved directly, there is no guarantee that the solution satisfies specific constraints. As an example, the actuators should respect their physical bounds at all time. To this end one can include constraints by formulating the problem as a quadratic constrained quadratic program (QCQP).

$$\arg\min_{\mathbf{c}} \quad \mathbf{c}^T\mathbf{J}^T\mathbf{J}\mathbf{c} - 2\mathbf{c}^T\mathbf{J}^T\mathbf{w} + \mathbf{w}^T\mathbf{w} \tag{13}$$

$$\text{s.t.} \quad \mathbf{b}_l \leq \mathbf{c} \leq \mathbf{b}_u \tag{14}$$

$$\mathbf{A}_{eq}\mathbf{c} = \mathbf{b}_{eq} \tag{15}$$

$$\mathbf{A}_{ineq}\mathbf{c} \leq \mathbf{b}_{ineq} \tag{16}$$

$$\forall i \quad \mathbf{c}^T\mathbf{H}_i\mathbf{c} + \mathbf{c}^T\mathbf{k}_i + d_i \leq b_{quad_i} \tag{17}$$

The following constraints are implemented:

- **Actuator constraints**: these are defined by (14).
- **Wafer positioning**: at all times the wafer offset, which is the average centroid distortion over all object points, should be zero. The constraint for wafer offset in the x direction looks like

  $$\mathbf{1}_{QM}^T\mathbf{D}_{x_p}\mathbf{J}\mathbf{c} = \mathbf{1}_{QM}^T\mathbf{D}_{x_p}\mathbf{w} \tag{18}$$

  where, for an arbitrary $a \in \mathbb{N}$, $\mathbf{1}_a = \begin{bmatrix}1 & \cdots & 1\end{bmatrix}^T \in \mathbb{R}^a$. Furthermore, if we denote $\mathbf{x}_p = \begin{bmatrix}x_p & y_p\end{bmatrix}^T$, then $\mathbf{D}_{x_p}$ is the matrix that implements

  $$\frac{1}{\mathrm{NA}}\frac{\partial w(\mathbf{x}_o, \mathbf{x}_p)}{\partial x_\mathrm{p}} \tag{19}$$

  Equation (18) is a linear equality constraint similar to (15).
- **Zero RBA modes in DM**: since the DM and RBA actuators are correlated, on some occasions RBA and DM corrections might work against each other. This results in an increase in actuator values and consequently modeling errors become more dominant. Fortunately, it is possible to force the DM actuators to only produce modes that are orthogonal to the RBA actuators sensitivities. As an example, take an arbitrary RBA influence function $\mathbf{j}_{rba} \in \mathbb{R}^{QM}$ and an arbitrary DM influence matrix $\mathbf{J}_{dm} \in \mathbb{R}^{QM\times N_{dm}}$. The undesired DM mode is obtained by fitting the RBA influence function onto the DM actuators:

  $$\mathbf{c}_{rba\to dm} = (\mathbf{J}_{dm}^T\mathbf{J}_{dm} + \mathbf{\Gamma}^T\mathbf{\Gamma})^{-1}\mathbf{J}_{dm}^T\mathbf{j}_{rba} \tag{20}$$

  in which $\mathbf{\Gamma}$ is set to perform both some conventional and smoothing Tikhonov regularization. Now the following equality constraint can be used to orthogonalize the DM and RBA actuators:

  $$\mathbf{c}_{rba\to dm}^T\mathbf{c}_{dm} = 0 \tag{21}$$
- **RMS WFE per point**: one can partition $\mathbf{J}$ as

  $$\mathbf{J} = \begin{bmatrix}\mathbf{J}_1^T & \cdots & \mathbf{J}_Q^T\end{bmatrix}^T \tag{22}$$

  in which $\mathbf{J}_q$ is the influence matrix for the WFE map of the qth object point. The residual RMS WFE of that object point is given by

  $$\mathbf{c}^T\mathbf{J}_q^T\mathbf{J}_q\mathbf{c} - 2\mathbf{c}^T\mathbf{J}_q^T\mathbf{w}_q + \mathbf{w}_q^T\mathbf{w}_q \tag{23}$$

  which can be used as a quadratic constraint of the form (17).

- **Centroid distortion per point in x and y**: calculating the centroid distortion, or overlay, in x and y is similar to (18) and can be implemented by two inequality constraints. For distortion in x these two equations look like

$$-b_{dist} \leq \mathbf{1}_M^T \mathbf{D}_{x_p,q} \mathbf{J}_q \mathbf{c} - \mathbf{1}_M^T \mathbf{D}_{x_p,q} \mathbf{w}_q \leq b_{dist} \tag{24}$$

where $\mathbf{1} \in \mathbb{R}^M$ and $\mathbf{D}_{x_p,q}$ implements (19) for the qth WFE map only. These two equations can be transformed into a single quadratic constraint similar to (17) where

$$\begin{aligned} \mathbf{H}_i &= \mathbf{J}_q^T \mathbf{D}_{x_p,q}^T \mathbf{1}_M \mathbf{1}_M^T \mathbf{D}_{x_p,q} \mathbf{J}_q & (25)\\ \mathbf{k}_i &= -2\mathbf{J}_q^T \mathbf{D}_{x_p,q}^T \mathbf{1}_M \mathbf{1}_M^T \mathbf{D}_{x_p,q} \mathbf{w}_q & (26)\\ d_i &= \mathbf{w}_q^T \mathbf{D}_{x_p,q}^T \mathbf{1}_M \mathbf{1}_M^T \mathbf{D}_{x_p,q} \mathbf{w}_q & (27)\\ b_{quad_i} &= b_{dist}^2 & (28) \end{aligned}$$

After constructing all these constraints it is possible to solve the QCQP in MATLAB. Since this is a convex problem, any local minimum is also a global minimum.[15] However, if the constraints are too restrictive, then the solution set is empty and the solver will not produce a useful solution. On many occasions it is not clear beforehand whether or not the problem is feasible using a certain MMAO configuration. Hence a QCQP approach does not serve our purpose. However, within the context of this paper, the first three linear constraints (14), (18) and (21) define a non-empty set. Hence the resulting linear constrained quadratic problem (LCQP) is feasible. Furthermore, by reformulating the problem into a goal attainment problem, all the constraints mentioned above can be used, which could lead to a solution that outperforms the LCQP solution.

5.2 Multi-objective optimization: Goal Attainment

By converting the QCQP problem in a multi-objective optimization problem, the goal attainment method is able to find a meaningful solution, even if the constraints cannot be met entirely.[16] This is done by adding a relaxation parameter ζ to each of the quadratic constraints and minimizing ζ. This is implemented using the MATLAB routine *fgoalattain*, which results in the following problem formulation:

$$\begin{aligned} \arg\min_{\zeta,\mathbf{c}} \quad & \zeta & (29)\\ \text{s.t.} \quad \forall i \quad & F_i(\mathbf{c}) - \nu_i \zeta \leq b_i & (30)\\ & \mathbf{b}_l \leq \mathbf{c} \leq \mathbf{b}_u & (31)\\ & \mathbf{A}_{eq}\mathbf{c} = \mathbf{b}_{eq} & (32) \end{aligned}$$

The relaxation parameter ζ is thus used to minimize the infinity norm over the ensemble of objectives (30). In this paper, for each of the 65 points constraints for RMS WFE and centroid distortion in x and y are included, leading to 195 unique objectives $F_i(\mathbf{c})$. Each scalar $\nu_i > 0$ is a user defined weight. By increasing the value of a specific weight, less emphasis is put on finding a solution that satisfies the corresponding constraint. The 65 constraints related to RMS WFE are quadratic. While it is possible to express centroid distortion using the linear equations described by (24), it turned out to be easier to control the behavior of *fgoalattain* if these constraints are used in their quadratic form. By using only quadratic constraints, all objectives behave similarly when violating their goals. Since for this paper $F_i(\mathbf{c})$ are all quadratic, the problem is convex.[15] It is important to realize that *fgoalattain* does not require the objectives to be convex, hence this solver might not be able to fully exploit the convex nature of the problem. Nevertheless, it is possible to provide *fgoalattain* with an analytical expression for the gradient of each objective, which considerably speeds up the optimization. When solving the goal attainment problem, the solution to the LCQP, with (14), (18) and (21) as constraints, is used as an initial guess.

6. SIMULATIONS, RESULTS AND INTERPRETATIONS

While in our previous study[9] the focus was on steady state performance only, for this paper transient behavior is also analyzed. The simulation settings were already introduced in table 1. Figure 4 shows the behavior of the

RMS WFE over time. The results are obtained using the LCQP approach, with the constraints defined by (14), (18) and (21) active. The label 'hot', refers to the uncontrolled POB. This figure shows that RBA corrections are able to reduce both the spread and the average value of the RMS WFE over the measured object points. However, RBA alone are not capable of meeting the requirement for RMS WFE, denoted in table 2, at any time instance. Although not shown here, it was verified that the same is true for the centroid distortion in x and y.

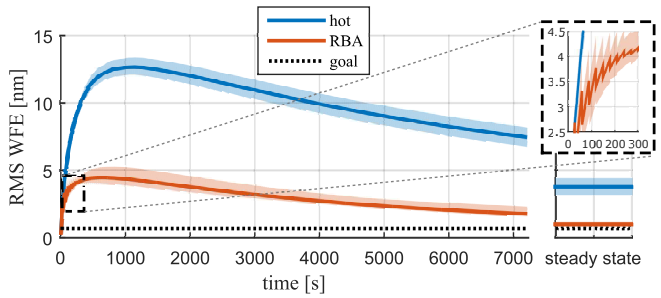

Figure 4: Transient behavior of the RMS WFE for the uncontrolled (hot) and RBA controlled system, optimized for total RMS WFE. The thick lines denote the average value for all measured object points. The shaded areas depict the range of values covered by the 65 object points analyzed. The sawtooth behavior in the enlarged area shows the controller tracking error. The results are obtained using the LCQP approach, with the constraints defined by (14), (18) and (21) active.

6.1 Choosing an initial MMAO configuration

Figure 4 shows that additional measures are necessary to get the optical performance to match the KPI bounds. The deformations are found to be most dominant on M1, especially during the first few minutes, so compensating for the deformation on M1 is assumed most effective. Analyzing the performance of the hot and RBA controlled POB showed that the worst case time instant is located at 1200 seconds. By directly fitting the thermal deformations for $t = 1200$ s onto various DM surface configurations, one can quickly get an indication on the DM properties needed to correct for the thermal deformations. There are two key properties to decide on: the actuator spacing and the FWHM of each actuator. The actuator spacing is parameterized as the number of actuators per pupil radius $\frac{r_{p,m_j}}{\Delta_{act}}$. Here, r_{p,m_j} denotes the average pupil radius at the jth mirror. The resulting RMS fit error on M1 as a function of both parameters is shown in Figure 5. This analysis is also carried out for M2 and leads to the initial settings for DM parameters shown in table 3.

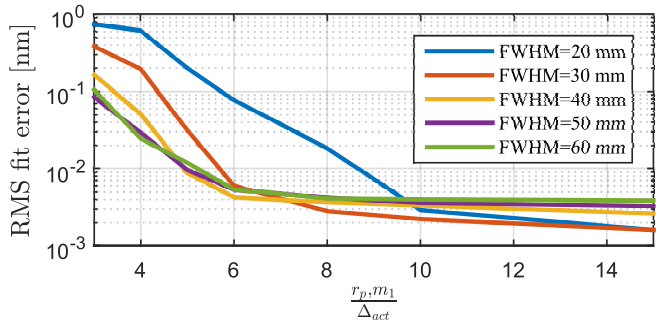

Figure 5: RMS fit error as a function of FWHM and actuator densitiy for the thermal deformation on M1 when $t = 1200$ s.

Table 3: Initial guess on DM actuator parameters.

	$r_{p,m_j}/\Delta_{act}$	FWHM [mm]	N_{act}
M1	6	40	422
M2	5	50	178

Table 4: Optimized DM actuator parameters.

	$r_{p,m_j}/\Delta_{act}$	FWHM [mm]	N_{act}
M1	4	40	205
M2	4	50	121

6.2 Optimizing the MMAO configuration

Figure 6 shows the performance over time of four DM controlled POB configurations for RMS WFE and centroid distortion in x and y. The plots show outlier performance, i.e. the infinity norm of the KPI is taken over all 65 measured WFE maps. In these plots, controller tracking errors, such as shown in Figure 4, are removed. Therefore, the remaining errors consists of modes that cannot be corrected by the configuration at hand. This way, the limitations of each AO configuration can be assessed. The results with the label *dense* refer to configurations based on the initially guessed parameters. However, as this figure shows, it is possible to reduce the number of DM actuators, without degrading the performance significantlym. The optimized parameters are shown in table 4. Looking at RMS WFE, only the configuration with both M1 and M2 is able to satisfy the bound with respect to RMS WFE. Note that at steady state all DM configurations suffice. For centroid distortion in the x-direction, different behavior emerges. Distortion in x is dominant over distortion in y. Initially, the former exceeds the bound of 1.35 nm for more than an hour if the optimization is done on total RMS WFE only, as the middle plot in Figure 6 shows. Furthermore, by comparing the dense with the optimized configuration, one sees that reducing the number of DM actuators does not change the performance notably. The optimized configuration is better in the sense that it reduces the number of DM actuators by almost a factor of 2, making the solution more cost-effective in practice.

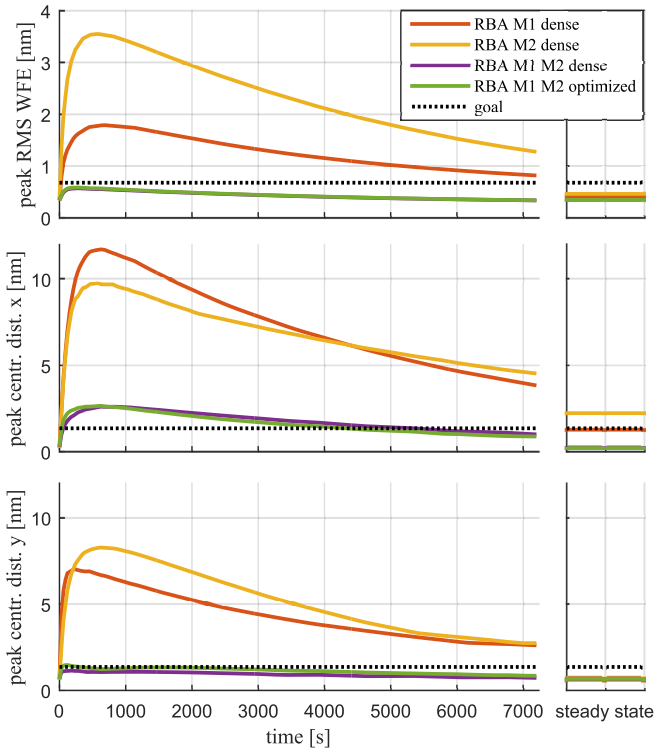

Figure 6: Transient behavior of 4 different RBA and DM controlled configurations. Controller tracking errors are removed. The label *dense* means the configuration is based on the initial guessed parameters, shown in table 3. The label *optimized* refers to the optimized DM parameters shown in table 4.The results are obtained using the LCQP approach, with the constraints defined by (14), (18) and (21) active

6.3 Optimization for design specific imaging criteria

Figure 6 also reveals why multi-objective optimization could potentially improve the performance beyond those obtained when only minimizing the total RMS WFE. The bound with respect to RMS WFE is met easily, while the bound for centroid distortion in x is not. The next step is to assess whether multi-objective optimization, by means of the MATLAB routine *fgoalattain* is able to get all measured object points within specs. When using the goal attainment method, one has to specify the weights ν_i to use in (30). Some manual tuning revealed

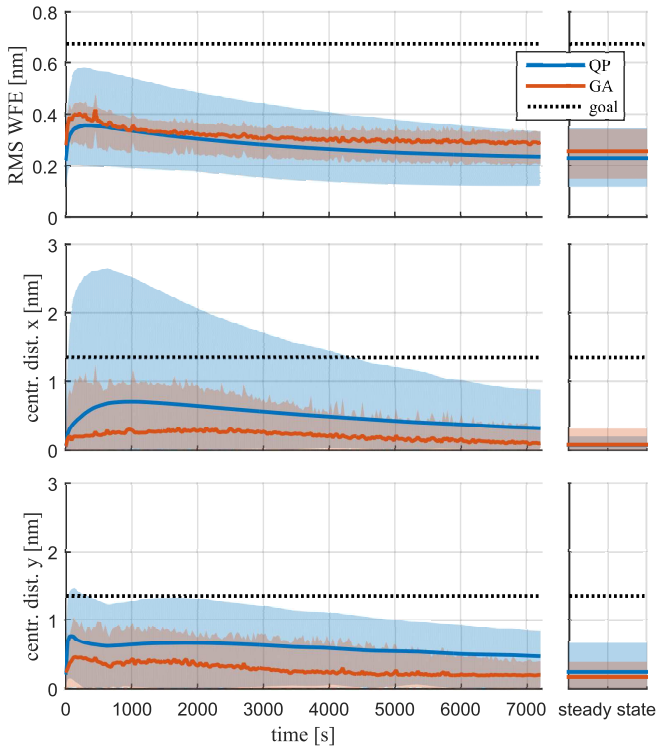

Figure 7: Performance comparison between only minimizing $\mathbf{w}_\epsilon$ (denoted by QP) and the goal attainment (GA) approach. The thick lines denote the average value for all measured object points. The shaded areas depict the range of values covered by the 65 object points analyzed. Controller tracking errors are removed. Note that the QP solution was found using the LCQP approach, with the constraints defined by (14), (18) and (21) active. The GA solution used the same linear constraints, but in addition, for each of the 65 object points, RMS WFE and centroid distortion in x and y are added as a quadratic objective.

that good results are obtained if the objectives related to RMS WFE get $\nu_i = 1$ and those related to centroid distortion get $\nu_i = 5$. This way, the optimization algorithm will only allow an increase of 0.2 nm in RMS WFE if that improves the centroid distortion length by 1 nm or more. Figure 7 shows a comparison between optimizing for total RMS WFE (QP) and multi-objective optimization (GA). In the latter, for each of the 65 object points three objectives exist: one for RMS WFE, one for centroid distortion in x, and another for centroid distortion in y. This leads to a total of 195 objectives. The figures clearly show that the goal attainment method is able to get the performance for all object points withing specs for all three KPI at all time instances.

7. CONCLUSIONS

This paper described how ideas from MCAO can be used to reduce the impact of thermally induced aberrations on the performance of an EUVL POB. To this end, a Gaussian DM model is implemented. This model is verified to be accurate enough to provide insight into the capabilities of a specific DM configuration within the simulation environment. Fast prototyping is possible by deriving the actuator sensitivities directly, based nominal ray locations and directions. Transient simulations of a multiphysics model have been performed to assess the thermo-mechanical behavior of the thermally deformed POB over time. For a use case with $P_{IF} = 1$ kW, the optical performance of several RBA and DM controlled configurations has been analyzed for a simulation time of 2 hours. A configuration with RBA and M1 and M2 as a DM yields superior performance. This configuration is able to meet the performance criteria much earlier in time, than the other configurations tested. Moreover, by using a multi-objective optimization procedure, the performance of each of the 65 object points analyzed satisfies all three different objectives at each measurement instance. This is not possible by just minimizing the ℓ_2-norm of the residual WFE.

REFERENCES

[1] ITRS, "International Technology Roadmap For Semiconductors - Lithography Summary." http://www.itrs.net/ITRS1999-2014Mtgs,Presentations&Links/2013ITRS/2013Chapters/2013Litho_Summary.pdf (2013).

[2] Peeters, R., Lok, S., Mallman, J., and van Noordenburg, M., "EUV Lithography: NXE platform performance overview," in [*Proc. of SPIE Vol. 9048*], SPIE, San Jose, California, USA (2014).

[3] Saathof, R., *Adaptive Optics to Counteract Thermal Aberrations*, PhD thesis, Delft University of Technology (2013).

[4] Haber, A., Polo, A., Maj, I., Pereira, S. F., Urbach, H. P., and Verhaegen, M., "Predictive control of thermally induced wavefront aberrations," *Opt. Express* **21**(18), 21530–21541 (2013).

[5] Hardy, J. W., [*Adaptive optics for astronomical telescopes*], vol. 53 (1998).

[6] Marchetti, E., Brast, R., Delabre, B., et al., "On-sky Testing of the Multi-Conjugate Adaptive Optics Demonstrator," *The Messenger* **129**, 8–13 (2007).

[7] Flicker, R., Rigaut, F., and Ellerbroek, B., "Comparison of multiconjugate adaptive optics configurations and control algorithms for the Gemini South 8-m telescope," in [*Adaptive Optical Systems Technology*], **4007**, 1032–1043, SPIE Optical Engineering Press, Munich, Germany (2000).

[8] Hudyma, R., "High numerical aperture ring field projection system for extreme ultraviolet lithography," (2000).

[9] Habets, M., Merks, R., Weiland, S., and Coene, W., "A Multiphysics Modeling Approach for Thermal Aberration Prediction and Control in Extreme Ultraviolet Lithography," in [*OSA meeting on Adaptive Optics (AO)*], AOM4B.2, Optical Society of America (2015).

[10] Andersen, T. and Enmark, A., [*Integrated Modeling of Telescopes*], Springer-Verlag, New York (2011).

[11] Ellerbroek, B. and Vogel, C., "Inverse problems in astronomical adaptive optics," *Inverse Problems* **25**(6) (2009).

[12] Redding, D. C. and Breckenridge, W. G., "Linearized ray-trace analysis," in [*Proc. SPIE*], **1354**, 216–221 (1991).

[13] Fusco, T., Conan, J.-M., Rousset, G., et al., "Optimal wave-front reconstruction strategies for multiconjugate adaptive optics," *J. Opt. Soc. Am. A* **18**(10), 2527–2538 (2001).

[14] Roux, B. L., Kulcsár, C., Mugnier, L. M., et al., "Optimal control law for classical and multiconjugate adaptive optics," *J. Opt. Soc. Am. A* **21**(7), 1261–1276 (2004).

[15] Boyd, S. and Vandenberghe, L., [*Convex Optimization*], Cambridge University Press (2004).

[16] Gembicki, F. and Haimes, Y., "Approach to performance and sensitivity multiobjective optimization: The goal attainment method," *IEEE Transactions on Automatic Control* **20**(6) (1975).